Physics – Uspekhi **68** (6) 537 – 550 (2025)

REVIEWS OF TOPICAL PROBLEMS PACS number: **74.78. – w**

Ising superconductivity

S.G. Ovchinnikov

DOI: https://doi.org/10.3367/UFNe.2024.06.039696

Contents

Abstract. We consider experimental and theoretical studies of Ising superconductivity. This new field in the physics of superconductivity was given impetus by the discovery of unusual properties in layered molybdenum disulfide (MoS_2) exhibiting an unprecedentedly high upper critical magnetic field B_{c2}, exceeding the paramagnetic Pauli limit six fold. It turns out that this is due to the properties of the crystal lattice of two-dimensional monolayers inducing Ising and Rashba spin–orbit coupling. Features of the crystal structure lead to a possible coexistence of singlet and triplet pairing and to the emergence of topological phases. Some options for searching for the Majorana fermion formations at the ends of long one-dimensional wires on the surface of an Ising superconductor are discussed.

Keywords: layered structures with triangular layers, Ising spin–orbit coupling, Rashba spin–orbit coupling, singlet and triplet Cooper pairs, topological states

1. Introduction

Since the discovery of graphene in 2004 [1], 2D nanomaterials have attracted much attention due to their unique physical and chemical properties and numerous potential applications. The most famous new types of nanomaterials include the transition metal dichalcogenide (TMD) family, *MX*enes, hexagonal boron nitride (h-BN), and many others. Ising superconductors, implemented in the TMD series, are a new and interesting class of materials that are unique both in their potential applications and in the new physics which encompasses unconventional superconductivity (the term was introduced by Mineev and Samokhin [2]), including topological phases.

As is known, strong magnetic fields suppress Cooper pairs with antiparallel spins. There are several mechanisms, the strongest of which is paramagnetic. It is associated with the splitting of band energies for electrons with spin-up and spin-down orientations. As a result, the external magnetic field cannot exceed the value of the so-called Clogston–Chandrasekhar paramagnetic limit B_P [3, 4]. The threshold field value in Tesla units is related to the critical temperature $T_c(0)$ in Kelvin units by the expression $B_P = 1.86T_c(0)$. For the convenience of readers, we explain that there are two mechanisms for suppressing superconductivity by an external magnetic field. The diamagnetic mechanism is associated with an increase in the energy of the superconducting state in a magnetic field by $H^2/8\pi$ [5], with the effect of the magnetic field on the normal state being neglected. In low-energy fields, the corrections to the energy of the normal state due to Pauli paramagnetism and Landau diamagnetism are significantly smaller than $H^2/8\pi$. However, as the field increases, the spin splitting of the bands in the normal metal increases, which leads to misorientation of the spins in the Cooper pair and to the Clogston–Chandrasekhar paramagnetic limit. The formation of critical fields in various types of superconductors was discussed in detail in book [6] and reviews [7–10].

We should emphasize that the magnetic field limitation does not apply to triplet pairing and the inhomogeneous Larkin–Ovchinnikov–Fulde–Ferrell (LOFF) state. Note that the paramagnetic limit is set for a bulk superconductor. For a thin film of thickness d in a parallel external field, it can be shown within the framework of the Ginzburg–Landau theory

S.G. Ovchinnikov
L.V. Kirensky Institute of Physics,
Federal Research Center Krasnoyarsk Science Center
of the Siberian Branch of the Russian Academy of Sciences,
Akademgorodok 50, str. 38, 660036 Krasnoyarsk, Russian Federation
E-mail: sgo@iph.krasn.ru

Received 15 May 2024, revised 20 June 2024
Uspekhi Fizicheskikh Nauk **195** (6) 569 – 583 (2025)
Translated by I.A. Ulitkin

that the critical field is [11]

$$B_{\rm k} = 2\sqrt{6}B_{\rm c2}\frac{\lambda}{d}\,. \qquad (1)$$

As the film thickness decreases, its critical field increases! At a penetration depth of $\lambda = 10d$, $B_{\rm c2}$ can be increased tens of times.

Soon after the discovery of superconductivity, the issue of its possible emergence in the two-dimensional case came to the fore. As early as 1938, Shalnikov [12] was the first to study thin superconducting films of lead and tin. Ising superconductivity is also observed in thin films. Note that, in this case, there is no contradiction with the known theoretical results on the impossibility of long-range order in two-dimensional systems or on the formation of an inhomogeneous Berezinskii–Kosterlitz–Thouless state. As will be shown below, even one monolayer of 2H-MoS_2 contains six atomic layers. Studies of superconductivity in monolayers of transition metal dichalcogenides began in the 2010s, the term 'Ising superconductivity' appeared in publications in 2015, and this area has nowadays developed both in breadth (various classes of TMDs have been studied) and in depth (the nature of the superconducting state formed under conditions of strong spin–orbit coupling is qualitatively clear). Therefore, a review of the results on Ising superconductivity is of interest.

2. Main experimental results of studies on Ising superconductivity

2.1 Features of crystal structure of transition metal dichalcogenides

The synthesis, structure, properties, and possible applications of quasi-2D transition metal compounds are described in detail in review [13] (however, without discussing superconductivity in these materials). Best known are the two main phases of MoS_2: the thermodynamically stable 2H phase and the metastable 1T phase (space group $P3m1$) [14], where H and T denote hexagonal and trigonal symmetries. Figure 1 shows structural polytypes of MoS_2 [15]. We begin our discussion with the simplest tetragonal structure of IT-MoS_2 (Fig. 1c). One can see that the unit cell contains two monolayers of MoS_2, each with three atomic planes; the upper and lower planes are formed by sulfur atoms, and the central one is formed by molybdenum. In the tetragonal 1T phase, one monolayer is located below the other. For the hexagonal structure of 2H-MoS_2 (Fig. 1a), the cell also contains two monolayers, but one is shifted relative to the other so that the Mo atom of the lower layer is located below the S atom of the upper layer. Finally, in the rhombohedral structure of 3R-MoS_2 (Fig. 1b), the unit cell contains three MoS_2 monolayers.

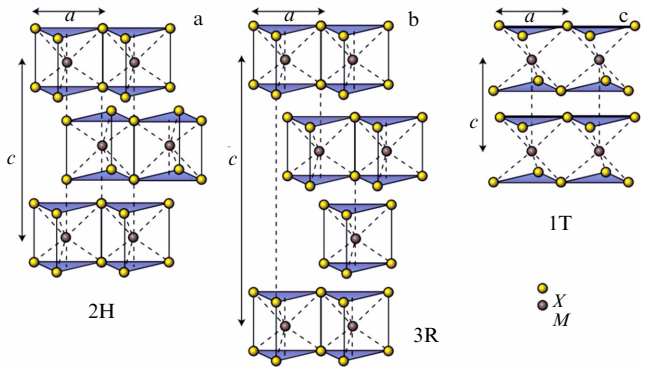

Figure 1. Schematics of structural polytypes of MoS_2: (a) 2H (hexagonal symmetry, two layers per repeat unit); (b) 3R (rhombohedral symmetry, three layers per repeat unit); and (c) 1T (tetragonal symmetry, one layer per repeat unit). Layers are vertically linked by weak van der Waals bonds [15].

A common feature of all layered transition metal dichalcogenides is a weak van der Waals bond between the monolayers. In this sense, there is a similarity with the structure of graphene and similar quasi-two-dimensional materials, in which thin films of different thicknesses can be exfoliated. Note the presence of polymorphism: in the S–Mo–S layers, the atoms can have trigonal prismatic (semiconductor 2H structure), octahedral (metallic 1T phase), and distorted octahedral configurations with zigzag Mo–Mo chains in the 1T′ phase [16].

2.2 Superconductivity in quasi-two-dimensional MoS_2 films

Under normal conditions, MoS_2 is a band semiconductor with a direct gap of 1.8 eV. In contrast to high-temperature semiconductor (HTSC) cuprates, where current carriers are formed by chemical doping; in the case of MoS_2, superconductivity was discovered during electrostatic doping. Thin MoS_2 flakes (up to 20 atomic layers) were separated from bulk 2H-MoS_2 single crystals using adhesive tape and transferred to the surface of HfO_2 grown on an Nb-doped $SrTiO_3$ substrate. Using external electrodes, a superconducting phase with a variable density of current carriers was formed in the surface layer under the action of an applied constant electric field.

Figure 2 shows an electron density–temperature phase diagram, in which the region of the superconducting phase has a dome shape, as in cuprates [17].

Figure 3 shows the temperature dependences of the upper critical field for a number of D1 and D24 samples from [18] at different $T_{\rm c}$ values. The superconducting state was observed in magnetic fields in the MoS_2 plane up to 32.5 T, exceeding

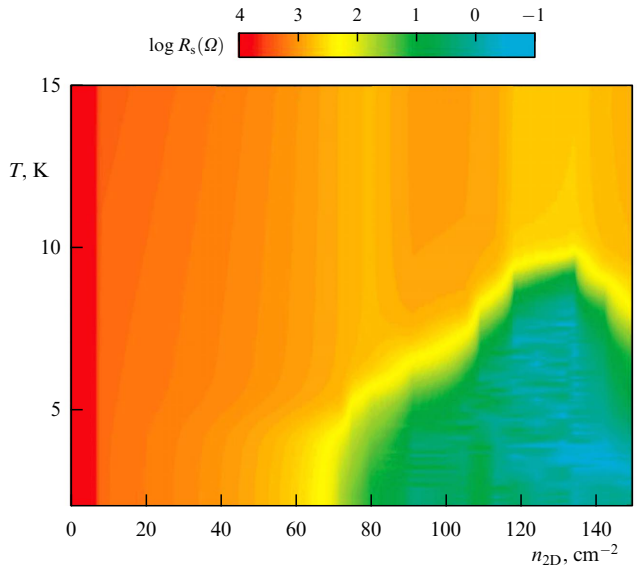

Figure 2. Phase diagram of 2H-MoS_2 showing electron density $n_{\rm 2D}$ [cm^{-2}] as a function of temperature. Superconducting phase is shown in green [17].

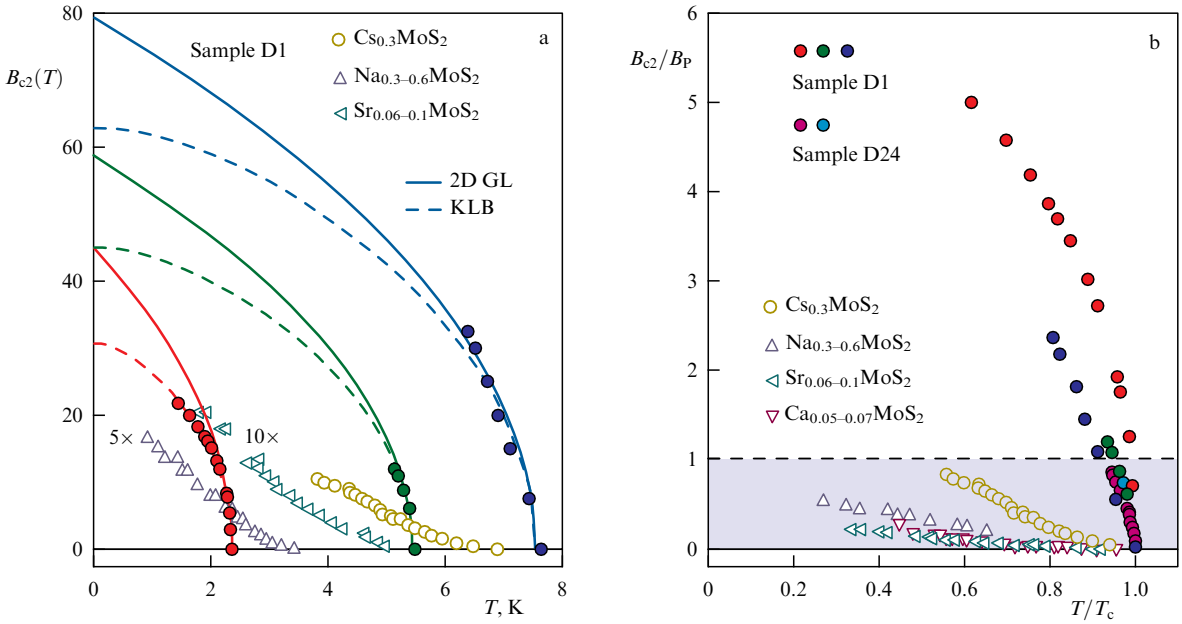

Figure 3. Temperature dependences of upper critical field of MoS_2 (a) for a series of samples D1 with different critical temperatures and (b) for three samples D1 and two samples D24 in dimensionless coordinates. Colored dots show experimental points, solid curves are their approximation according to Ginzburg–Landau (GL) model, and dashed curves are their approximation according to Klemm–Luther–Beasley (KLB) model. Fields below paramagnetic limit are shaded. For intercalated samples, paramagnetic limit is not reached [18].

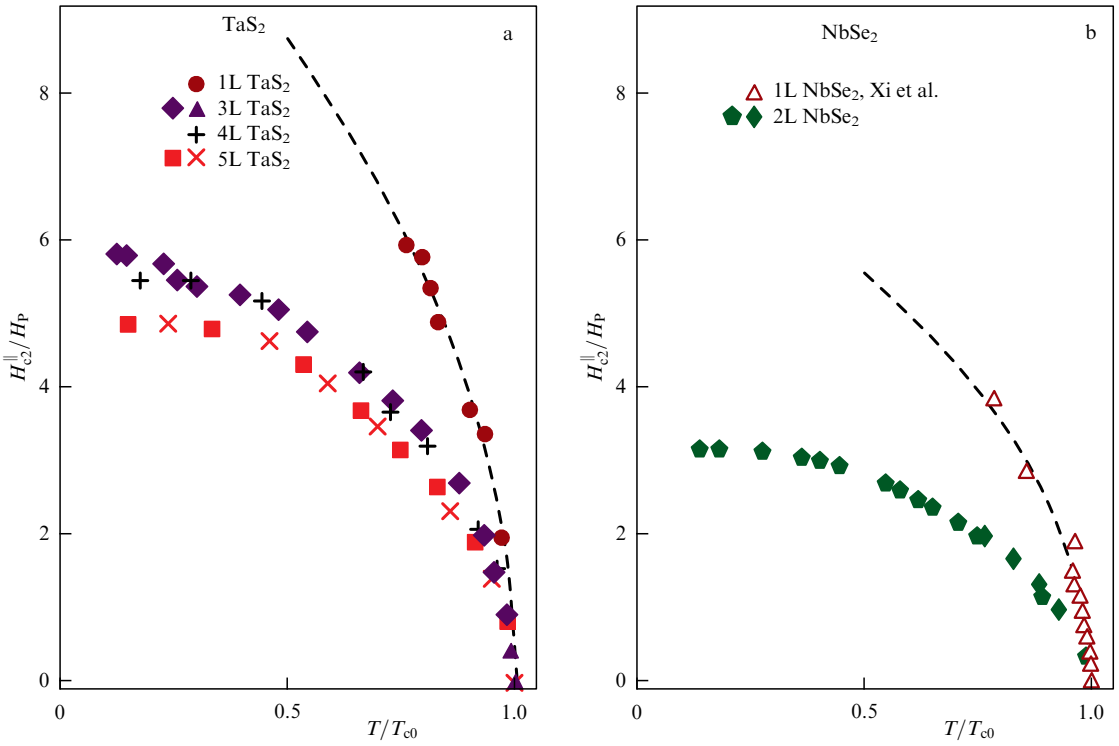

Figure 4. Effect of number of monolayers on upper critical field in (a) TaS_2 and (b) $NbSe_2$ (borrowed from [22]).

the paramagnetic limit by a factor of five. The figure also presents data for a number of MoS_2 samples intercalated with Cs, Na, and Sr, for which the critical fields B_{c2} lie below the paramagnetic limit. It was Lu et al. [18] who introduced the term 'Ising superconductivity.' Its meaning will be explained below in Section 3.2. In similar MoS_2 samples with electrostatic doping, a critical field of 52 T was observed at a temperature of 1.5 K [19].

2.3 Comparison with other layered transition metal dichalcogenides

Some transition metal dichalcogenides are intrinsic superconductors, such as $NbSe_2$, NbS_2, $TaSe_2$, and TaS_2 [20]. MoS_2, $MoSe_2$, and WSe_2 are dielectrics, but superconductivity in them can be induced either by intercalation with alkali metals or by injection of electrons from an external electrode. Monolayers of 2H-WSe_2 were also obtained in the super-

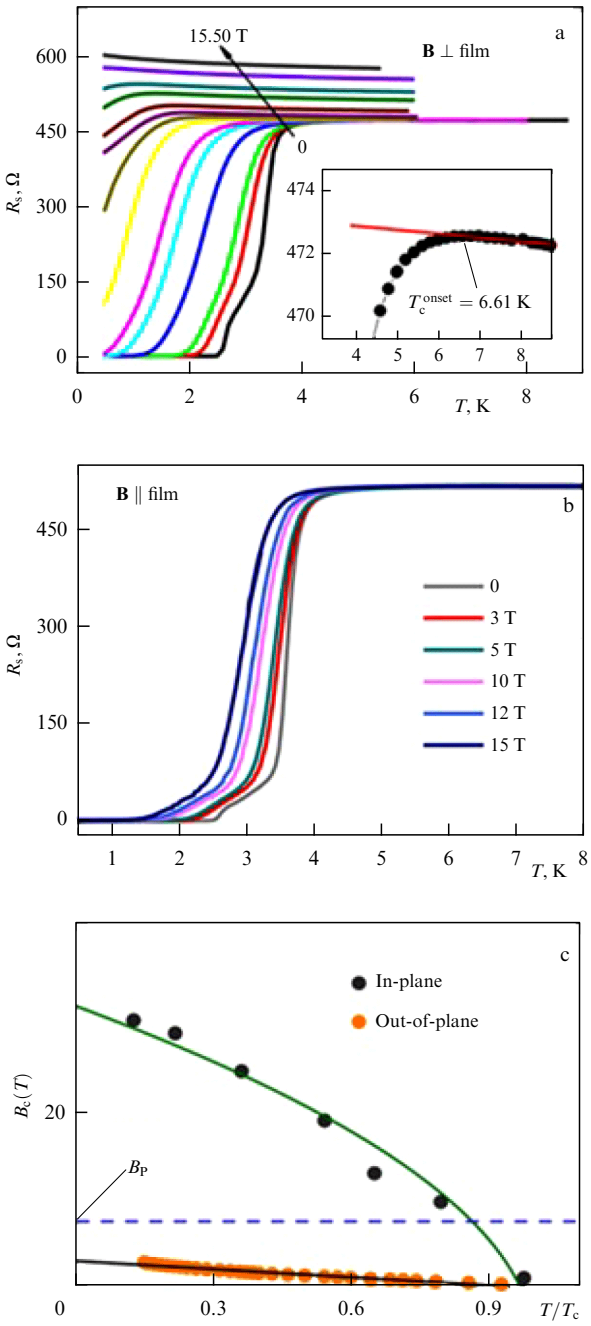

Figure 5. Temperature dependences of resistance in (a) transverse and (b) longitudinal magnetic fields of epitaxial $NbSe_2$ monolayer and (c) upper critical field (borrowed from [23]).

conducting state below $T_c = 3$ K, with a critical field B_{c2} exceeding the Pauli limit six-fold [21].

De la Barrera et al. [22] obtained important data on the dependence of the properties of TMD films on the number of monolayers (Fig. 4). For samples of 2H-TaS_2 with 1 to 5 monolayers and 2H-$NbSe_2$ with 1 and 2 monolayers, the transport properties in strong magnetic fields and the temperature dependences of the upper critical field were measured. A six- and four-fold excess of the paramagnetic limit for 2H-TaS_2 and 2H-$NbSe_2$ samples, respectively, was revealed, and the critical fields in both cases sharply decrease when going from one monolayer to two or more. This experiment most clearly demonstrates the two-dimensional nature of superconductivity in TMDs.

It is of interest to compare the superconducting properties of surface layers of bulk MoS_2, in which the carriers are pumped by an external electric field, and the properties of the intrinsic superconductor $NbSe_2$, whose atomically smooth monolayer 0.6 nm in thickness was grown on a 6H-SiC(0001) substrate coated with a bilayer of graphene using molecular beam epitaxy [23]. The $NbSe_2$ monolayer consists of two Se–Nb–Se layers. For *ex situ* measurements, the film was covered with a 20-nm-thick protective layer of amorphous Se.

Figure 5 shows the temperature dependences of the electrical resistance in a magnetic field (a) across and (b) along the monolayer surface, as well as (c) the upper critical fields for these directions. Extrapolation to zero temperature yields a value of the upper critical field $B_{c2} = 2.16$ and 32.43 T for the transverse and longitudinal fields, respectively. The paramagnetic limit is $B_P = 6.37$ T and is exceeded more than five times for the longitudinal field.

While external electron pumping is needed to initiate superconductivity in the original 2H-MoS_2 semiconductor [17], the 1T- and 1T′-MoS_2 metallic polytypes demonstrate superconductivity upon intercalation with potassium at a critical temperature of $T_c = 2.8$ and 4.6 K, respectively [24]. It is worth noting that intercalation of K in this case leads simultaneously to both structural and superconducting transitions. The expansion of the class of superconducting TMDs expands the possibilities of finding applications for this important class of new materials [13, 25, 26].

Before discussing the properties of Ising superconductors in detail, it is appropriate to ask the questions: Do only large values of the critical magnetic fields make this class of materials interesting? Do they have other interesting and unusual properties? The answer to both questions is certainly affirmative. First, due to the Ising spin–orbit coupling (SOC), the nature of which will be explained below, the coexistence of spin-singlet and spin-triplet pairing is possible, as expected in [27, 28]. As will be discussed below, spin-triplet Cooper pairs can be formed by electrons with parallel spins. If a thin wire is placed on such a superconductor, then, due to the proximity effect, Cooper pairs with parallel spins can also be induced in it, which in the presence of a magnetic field in the plane of the sample can lead to the formation of Majorana fermions at the ends of the wire [29]. Thus, the study of Ising superconductivity allows, in addition to potentially interesting technological applications, modern topical fundamental problems of condensed matter physics to be explored.

3. Features of electronic structure and mechanisms for formation of superconducting phase

3.1 Density functional theory and tight-binding model

The relationship between the crystal structure and the observed optical and electrical properties of MX_2 compounds, which include TMDs, was discussed as early as 1969 [30] (see also review [13]). Calculations of the electronic structure within the framework of first-principles methods of density functional theory (DFT) have now reached a level that allows us to trace the evolution of the band structure of thin single-crystal films as functions of the number of monolayers. Kuc et al. [31] performed such calculations for MoS_2 and WS_2.

Figure 6 shows the results of calculations of the band structure of various WS_2 modifications within the framework

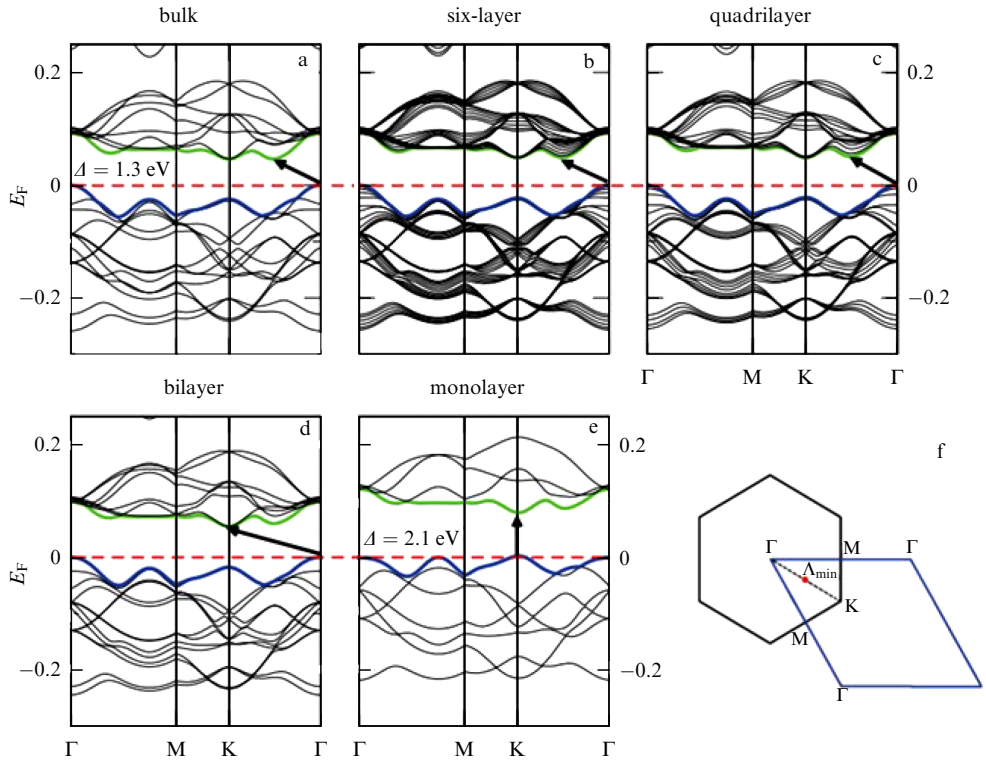

Figure 6. Electronic structures of different modifications of WS_2: (a) bulk, (b) six-layer, (c) quadrilayer, (d) bilayer, and (e) monolayer. (f) Two-dimensional Brillouin zone (borrowed from [31]).

of DFT with an exchange–correlation potential in the GGA-PBE approximation [31]. It can be seen that changes in the band structure upon transition from a bulk crystal to films with a thickness of 6, 4, and 2 monolayers are insignificant. For all these materials, the state of a semiconductor with an indirect gap and the top of the valence band at the Γ point and the bottom of the conduction band in the middle of the ΓM direction at the Λ point is realized (the Brillouin zone is also shown in Fig. 6). A sharp difference is observed for a monolayer, where the semiconductor gap becomes straight, with extrema at the top of the valence band and at the bottom of the conduction band at the K point. The same situation occurs for an MoS_2 monolayer.

For bulk 2H-$NbSe_2$ crystals and thin layers, the electronic structure was calculated by Calandra et al. [32] and Lian et al. [33], who also discussed the possibility of forming a dielectric phase due to a state with a charge-density wave (CDW). The CDW state in 2H-$NbSe_2$ was experimentally observed in [34, 35]. As is known, these phases are formed due to the peculiarities of the Fermi surface topology [36, 37] and have no direct relation to the formation of Ising superconductivity. Nevertheless, their mutual influence is manifested in some experiments, which will be considered below in Section 3.4.

Figure 7 compares the results of theoretical calculations of the electronic structure of $NbSe_2$ with the experimental data of angle-resolved photoelectron spectroscopy (ARPES). These data show not only the electron spectrum $E(k)$, but also the spectral weight of each state with the given wave vector and energy [38]. Figures 7a and 7b illustrate the measured dispersion laws of electrons along the K−Γ−M direction of the Brillouin zone for (a) intercalated and (b) nonintercalated samples; the calculated dispersion laws are presented in Figs 7c and 7d. The metallic state and the dielectric gap are visible in Fig. 7b and Fig. 7a, respectively.

Many theoretical calculations of the electronic structure of various TMDs have been published in connection with the discussion of the mechanism of the superconducting state; they will be discussed below.

3.2 Nature of Ising and Rashba spin–orbit coupling

Since strong spin–orbit coupling plays an important role in Ising superconductivity, we will consider the crystal structure and discuss in more detail the lattice symmetry of the MoS_2 monolayer (Fig. 8).

The most important symmetry operations for such a structure include

(i) rotations by $2\pi/3$ around the vertical axis C_3;

(ii) mirror symmetry in the layer (K ↔ −K inversion in the plane) is broken by the triangular structure in the layers, while in the 2H-MoS_2 crystal with two monolayers in the cell, the center of three-dimensional inversion is preserved; and

(iii) horizontal mirror plane σ_h (broken by the surface or substrate).

These symmetry violations are a physical reason for the appearance of the Ising-type and Rashba-type SOCs.

It is intuitively clear that the spin–orbit coupling for an electron with a wave vector $\mathbf{k}$, moving in an electric field $\mathbf{E}$, is proportional to $\mathbf{k} \times \mathbf{E} \cdot \boldsymbol{\sigma}$, where $\boldsymbol{\sigma}$ is the Pauli matrix. In an MoS_2 monolayer with broken mirror symmetry in the layer, the field $\mathbf{E}$ can exist in the plane of the monolayer. For an electron with a vector $\mathbf{k}$ in the plane of the monolayer, the product $\mathbf{k} \times \mathbf{E}$ is directed across the layer. The spins are oriented along the z-axis. This is how the Ising SOC manifests itself.

In a monolayer on a substrate, the translational invariance in the transverse direction is violated by the presence of an interface between the media, which leads to the possibility of the existence of a field $\mathbf{E}$ across the layer; the vector $\mathbf{k} \times \mathbf{E}$

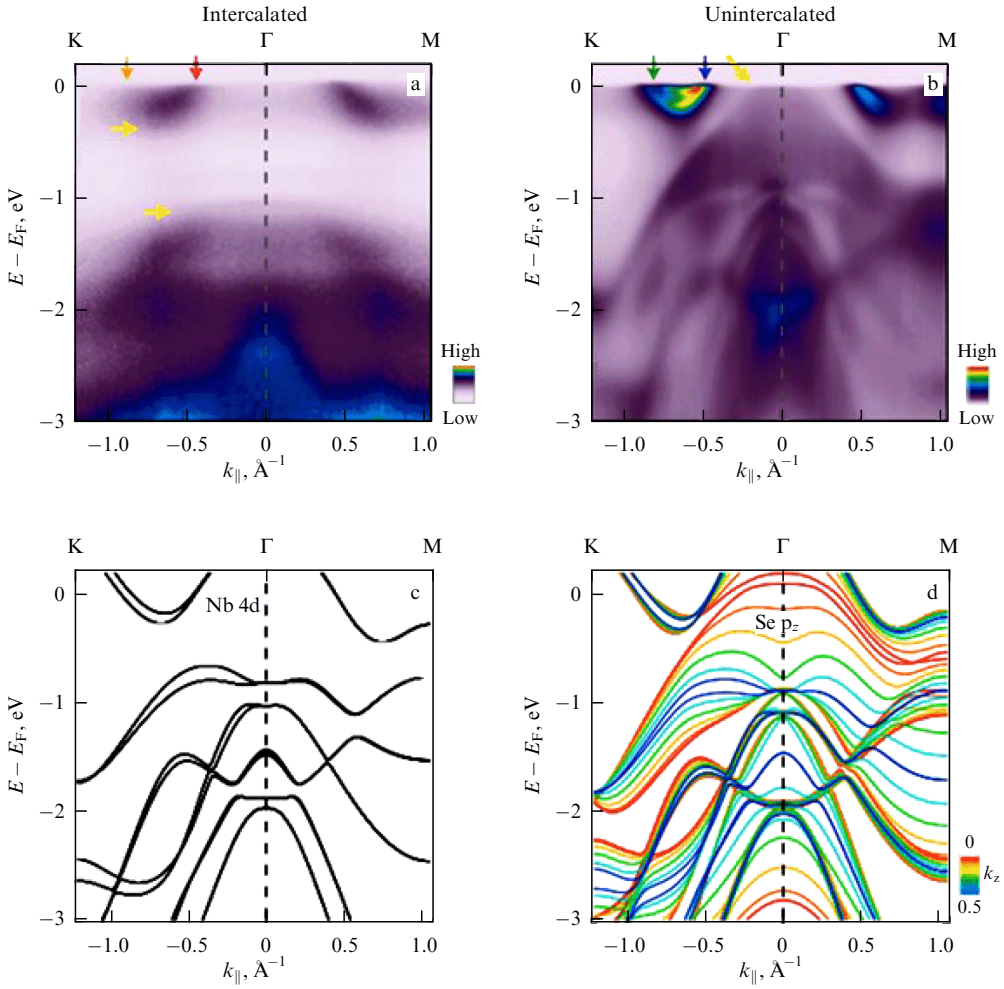

Figure 7. Comparison of results of theoretical calculations for electronic structure of $NbSe_2$ with ARPES experimental data. (a, b) Measured dispersions of electrons along K – Γ – M direction of Brillouin zone for (a) intercalated and (b) unintercalated samples. (c, d) Calculated dispersions. Metallic state is visible in panel b and dielectric gap, in panel a. Calculated spectrum in panel c for $k_z = 0$ corresponds to a monolayer. Data for bulk metallic sample in panel d show a series of calculations with different k_z from 0 to 0.5, corresponding to a monolayer and a bulk crystal (borrowed from [38]).

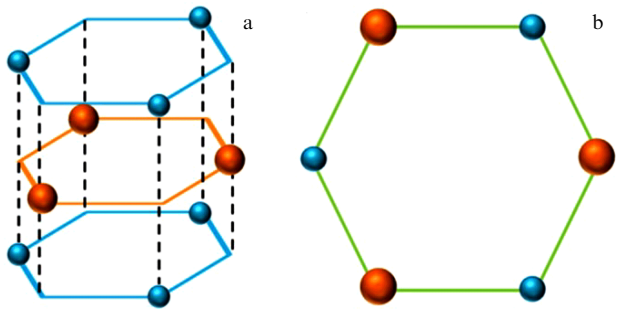

Figure 8. (a) Crystal structure of MoS_2 monolayer and (b) its top view. Smaller spheres from upper and lower layers represent sulfur atoms, and larger ones from middle layer represent molybdenum. Inversion center in layer plane is absent [15].

lies in the monolayer, and the Rashba SOC energy orients the spins in the plane and can be written as $k_x\sigma_y - k_y\sigma_x$. Both types of SOC operate in experiments with monolayers of MoS_2, $NbSe_2$, and other TMDs.

These qualitative considerations are confirmed by band calculations [39], the authors of which proposed a simplified tight-binding model for states near the top of the valence band and the bottom of the conduction band. The top of the valence band is formed mainly by $d_{x^2-y^2}$ and d_{xy} atomic orbitals of the Mo atoms. The bottom of the conduction band is mainly due to d_{z^2} atomic orbitals of the Mo atoms. Based on first-principles calculations, Kormányos et al. [39] constructed an effective low-energy Hamiltonian (2) describing the SOC effects for the top of the valence band:

$$H_{vb}^{so} = -\tau\Delta_1^v S_z + 0.5\Delta_2^v(1 + \tau S_z)\,. \qquad (2)$$

Here, $\tau = +1/-1$ for different K and K′ valleys. The calculations in [39] within the framework of DFT for the valence band yielded a spin–orbit gap of $2\Delta_1^v - \Delta_2^v = 146$ meV. For the bottom of the conduction band, a more cumbersome expression was obtained due to multi-band contributions to the expressions $L_-S_+ + L_+S_-$. We do not present it, since the calculation [39] yielded an SOC value of 3 meV for the bottom of the conduction band. The Ising SOC has opposite signs for the K and K′ valleys and preserves symmetry with respect to time inversion.

Near the K points of the Brillouin zone, the electron Hamiltonian in the normal phase for a monolayer of MoS_2 in the presence of an external magnetic field **B** can be

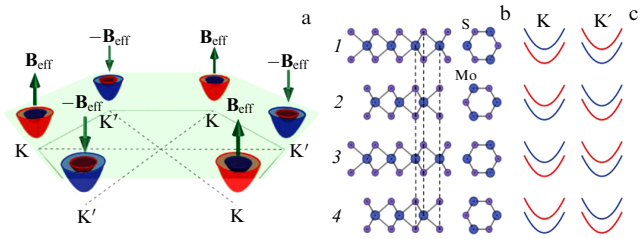

Figure 9. Effect of Ising spin–orbit coupling on electronic structure in MoS_2. (a) Electron pockets at K and K′ points with an effective field $\mathbf{B}_{\rm eff}$ and $-\mathbf{B}_{\rm eff}$ (green arrows). (b) Side (left) and top (right) views of four upper layers. Symmetry with respect to inversion is violated in each layer. (c) Band splitting due to $\mathbf{B}_{\rm eff}$; up and down spin directions are shown in blue and red [18].

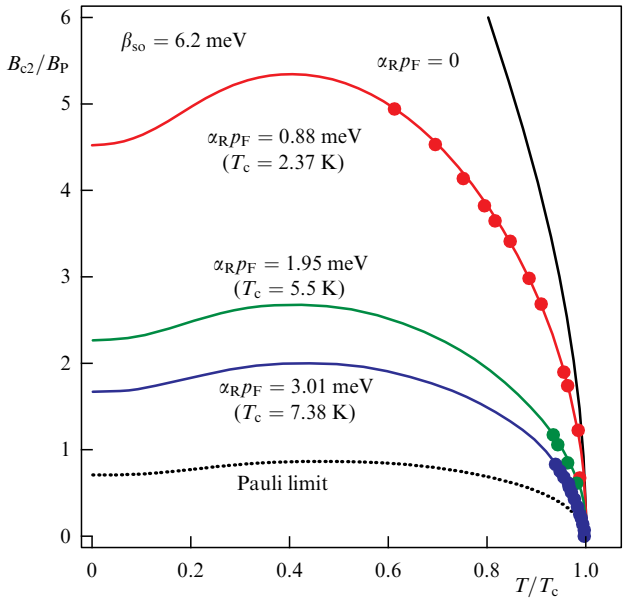

Figure 10. Effect of Ising and Rashba spin–orbit coupling on temperature dependence of critical field B_{c2}/B_P for MoS_2 samples with different critical temperatures. Ising SOC parameter is fixed at $\beta_{so} = 6.2$ meV; Rashba SOC parameter α_R was varied to match the experimental data. Dashed black curve is calculated in absence of SOC and shows paramagnetic limit (called the Pauli limit by the authors), which is exceeded by a factor of six by that on the red curve (borrowed from [18]).

written as [40]

$$H_0(\mathbf{k} + \tau\mathbf{K}) = \varepsilon_k + \tau\beta_{so}\sigma_z + \alpha_R \mathbf{g}_R \boldsymbol{\sigma} + \mu_B \mathbf{B}\boldsymbol{\sigma}. \qquad (3)$$

Here, $\varepsilon_k = k^2/(2m) - \mu$, $\mathbf{k} = (k_x, k_y, 0)$, and $\mathbf{K}$ is the wave vector in the K and K′ valleys. The second term describes the Ising SOC with $\beta_{so} = 6.2$ meV and orients the spins across the layer in opposite directions for the K and K′ valleys. The third term is responsible for the Rashba SOC with the vector $\mathbf{g}_R = (k_y, -k_x, 0)$ [41]. The last term in (3) is responsible for the Zeeman effect, and $\boldsymbol{\sigma}$ are the Pauli matrices.

The effect of the Ising SOC on the electronic structure of the MoS_2 film is shown in Fig. 9 [18].

An important effect is the removal of spin degeneracy in the K and K′ valleys. Assuming an s-type superconducting gap $\Delta_\Gamma(k) = \Delta_0 i\sigma_y$, Lu et al. [18] calculated the temperature dependences of the upper critical field for a number of samples with different values of the critical temperature with variable parameters of the Rashba SOC (Fig. 10). One can see

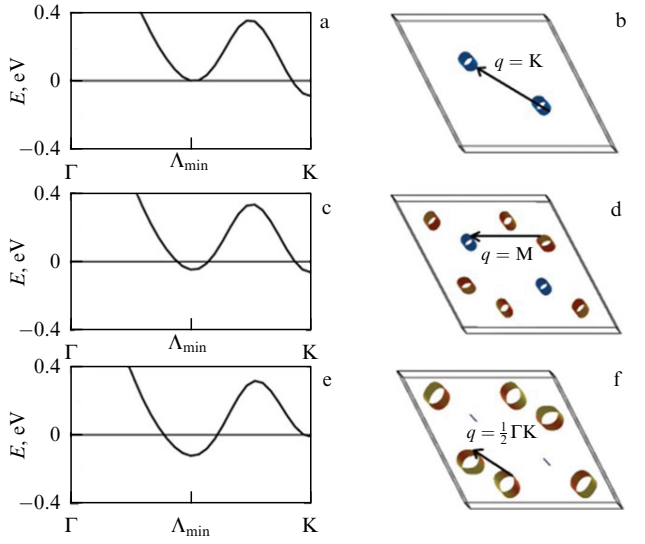

Figure 11. Changes in conduction band, Fermi surface, and wave vector of a phonon participating in EPC at different carrier densities in an MoS_2 monolayer for (a, b) 0.03, (c, d) 0.10, and (d, f) 0.22 electrons per formula unit. (Borrowed from [42].)

that, the smaller the Rashba SOC, the lower T_c and the higher B_{c2}.

3.3 Mechanisms of superconducting pairing

Ge and Liu [42] considered the electron–phonon mechanism of superconductivity in the electron-doped monolayer of MoS_2 within the framework of the DFT. They observed a weak electron–phonon coupling (EPC) at a low doping level. With an increase in the electron density, the EPC parameter rapidly increases, but then begins to decrease with further doping. Thus, Ge and Liu [42] were able to qualitatively explain the presence of a superconducting dome in the phase diagram $T_c(n)$ in Fig. 2. As the electron density increased, both the band structure and the characteristic wave vector of phonons changed, making the main contribution to the formation of the EPC (Fig. 11).

In subsequent first-principles calculations of the electronic structure, Das et al. [43] found that, for $NbSe_2$, the value of T_c obtained due to the EPC significantly exceeds the experimental one. Calculations taking into account spin fluctuations revealed six sharp peaks on wave vectors like the $\mathbf{q} = (0.2, 0, 0)$ type (Fig. 12).

For a monolayer, the spin susceptibility turned out to be 1.5 times greater than that for bulk $NbSe_2$ [44]. Simultaneous consideration of the EPC and spin-fluctuation contribution led to a partial suppression of the EPC mechanism and agreement between the calculated T_c value and the experimental data [45].

Roldán et al. [46] simultaneous took into account the EPC and Coulomb interaction and their contributions to intravalley (Fig. 13a) and intervalley (Fig. 13b) scattering processes. The LO phonons and screened Coulomb interaction (Fig. 13c) participate in pairing during intravalley scattering. The contribution to the intervalley scattering (Fig. 13d) is made by the same LO phonons, as well as the homeopolar mode of oscillations of S atoms across the layer and the local part of the Coulomb interaction U_{4d}. Estimates showed the dominant contribution of the Coulomb interaction to the intervalley pairing constant at $\lambda_{inter} > 0$, and that the s-gap in

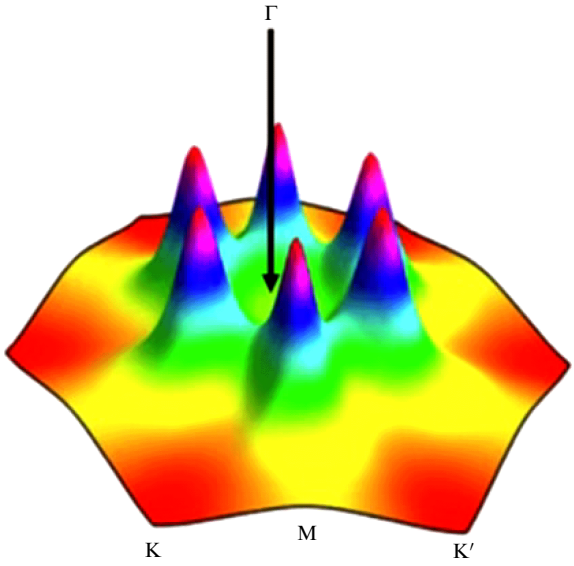

Figure 12. Spin susceptibility of $NbSe_2$ with sharp maxima at wave vectors $\mathbf{q} = (0.2, 0, 0)$. (Borrowed from [44].)

different valleys should have opposite signs (Fig. 13e). An alternating $d_{x^2-y^2}$ gap is also possible (Fig. 13f). However, estimates of the value of T_c for the last phase showed that its value is too small and it is unlikely that the phase is realized in MoS_2.

4. Topological phases and possible Majorana states in a thin magnetic rod on surface of Ising superconductor

To construct the theory of superconductivity, we will use Hamiltonian (3) for the normal state of MoS_2. The classification of possible superconducting phases in MoS_2 according to irreducible representations of the C_{3v} group is shown in the table.

For the one-dimensional A_1 and two-dimensional E representations of the C_{3v} group, the order parameter has the form

$$\Delta_\Gamma(\mathbf{k}) = \begin{cases} \left[S_{A_1,1}\psi_{A_1}(0) + S_{A_1,2}\psi_{A_1}(\mathbf{k}) + \right. \\ \quad \left. t_{A_1,z}\mathbf{d}_{A_1,z}\boldsymbol{\sigma} + t_{A_1,xy}\mathbf{d}_{A_1,xy}\boldsymbol{\sigma}\right] i\sigma_y\,, & \Gamma = A_1, \\ \sum_{m=\pm}\left[S_{E,m}\psi_{E,m} + t_{E,m}\mathbf{d}_{E,m}\boldsymbol{\sigma}\right] i\sigma_y\,, & \Gamma = E\,. \end{cases} \quad (4)$$

For the A_1 representation, ψ_A describes a standard s-type Cooper pair, and $\mathbf{d}_{A_1,z}(\mathbf{k}) = -\mathbf{d}_{A_1,z}(-\mathbf{k})$ is the spin-triplet pair arising due to the triangular lattice of Mo atoms. Roldán et al. [46] pointed out a possibility of forming a spin-triplet s-phase. The term $\mathbf{d}_{A_{1,xy}}\boldsymbol{\sigma} \sim \sigma_x k_y - \sigma_y k_x$ in formula (4) describes the spin-triplet $p + ip$ phase, which is stabilized by the Rashba SOC.

For the two-dimensional E representation, the parity condition $\psi_{E,m}\{\mathbf{k}\} = \psi_{E,m}\{-\mathbf{k}\}$ is met. Near the $\pm$K points, these pairs have a $p + ip$ character. Superconductivity with the order parameter symmetry $p + ip$ was previously discussed for Sr_2RuO_4 [47, 48]. Similar phases are known in noncentrosymmetric superconductors [49–51] and are topological superconductors. In the case of the E phase in MoS_2 with the order parameter $\Delta_\Gamma = S_{E,+}\psi_{E,+}i\sigma_y$, the symmetry with respect to time inversion is violated.

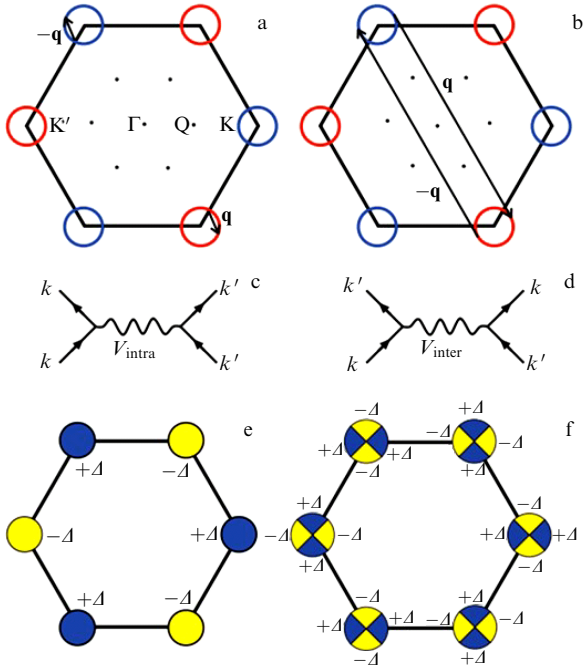

Figure 13. (a, c) Intravalley and (b, d) intervalley scattering processes leading to formation of Cooper pairs in paper [46]. (e) s-type phases with opposite signs of order parameter in different valleys and (f) phases with a $d_{x^2-y^2}$ gap are possible.

Table. Symmetry classification of possible pairing phases for monolayer MoS_2 (from [40]).*

Γ	Singlet	Triplet
A_1	$\psi_{A_1}(0) = C(\mathbf{k}=0)$ $\psi_{A_1}(\mathbf{k}) = C(\mathbf{k})$	$\mathbf{d}_{A_{1,z}} = S(\mathbf{k})z$ $\mathbf{d}_{A_{1,xy}} = S_-(\mathbf{k})x_+ - S_+(\mathbf{k})x_-$
E	$\psi_{E,+}(\mathbf{k}) = C_+(\mathbf{k})$ $\psi_{E,-}(\mathbf{k}) = C_-(\mathbf{k})$	$\mathbf{d}_{E,+} = S_+(\mathbf{k})z$ $\mathbf{d}_{E,-} = S_-(\mathbf{k})z$

* Following notations are introduced:

$$C(\mathbf{k}) = \sum_{j=1}^{3}\cos(\mathbf{kR}_j)\,, \quad S(k) = \sum_{j=1}^{3}\sin(\mathbf{kR}_j)\,,$$

$$C_+(\mathbf{k}) = \sum_{j=1}^{3}\omega^{j-1}\cos(\mathbf{kR}_j)\,, \quad S_+(\mathbf{k}) = \sum_{j=1}^{3}\omega^{j-1}\sin(\mathbf{kR}_j)\,,$$

$$C_-(\mathbf{k}) = C_+^*(\mathbf{k})\,, \quad S_-(\mathbf{k}) = S_+^*(\mathbf{k})\,.$$

Phase factor is $\omega = \exp(2\pi i/3)$. Bonding vectors of Mo atoms are $R_1 = \alpha x$, $R_2 = \alpha(-x/2 + \sqrt{3}y/2)$, $R_3 = \alpha(-x/2 - \sqrt{3}y/2)$ with lattice constant $\alpha = 1$. Also introduced are $x_+ = (x + iy)/\sqrt{2}$ and $x_- = (x - iy)/\sqrt{2}$.

The last of the possible superconducting phases in the general structure (4) is given by the vector order parameter $d_{E,\pm}(\mathbf{k} + \varepsilon\mathbf{K}) \cong -3/4(k_x \pm ik_y)\hat{z}$ and is a spin-triplet phase with p-type pairing, similar to the A phase of ^{3}He. As shown by Yuan et al. [40], this phase is energetically unfavorable for MoS_2.

Research into materials with special topological phases—topological insulators and topological superconductors—began quite a long time ago [52–57]; topological superconductivity and Majorana states in low-dimensional systems have been recently reviewed by Val'kov et al. [58]. Such phases are characterized by a topological invariant (TI), or

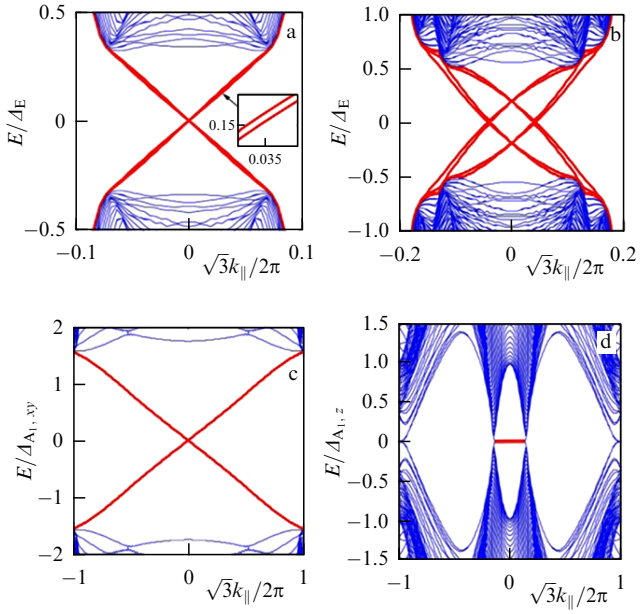

Figure 14. Electron spectra in tight-binding model for infinitely long thin strip of MoS_2 with different possible topological states: (a, b) in spin-singlet $p+ip$ E phase, where time inversion is violated; (a) $\mu = 0$ and $N_{\text{Chern}} = 2$, (b) $\mu = 4$ and $N_{\text{Chern}} = 4$; edge states are highlighted in red; (c) in $\mathbf{d}_{A_1,xy}$ spin-triplet $p+ip$ phase there are Majorana edge states; and (d) s-wave singlet in $\mathbf{d}_{A_1,z}$ topological phase with Majorana flatbands. (Borrowed from [40].)

Chern number [59],

$$N_{\text{Chern}} = \frac{1}{2\pi}\sum_{E_{n<0}}\int \mathrm{d}^2\mathbf{k}\,(\partial_x\alpha_y^n - \partial_y\alpha_x^n)\,, \quad \alpha_i^n = -\mathrm{i}\langle n,\mathbf{k}|\partial_{\mathbf{k}i}|n,\mathbf{k}\rangle\,.$$

Calculations [40] yielded the following values of the Chern number for MoS_2: $N_{\text{Chern}} = 2$ for $|\mu| < |\beta_{\text{so}}|$, $N_{\text{Chern}} = 4$ for $\mu > |\beta_{\text{so}}|$, and $N_{\text{Chern}} = 0$ for large negative values of μ.

Nonzero TI values indicate the formation of surface or edge states. The relationship between topological insulators and topological superconductors manifests itself in the existence of a gap in the spectrum of bulk excitations and in the formation of surface conducting states. In the simplest case of free electrons, all topological materials can be classified with respect to three types of symmetry: electron–hole, chiral, and time inversion. However, the mechanisms for the occurrence of a gap in the excitation spectrum and the structure of edge excitations differ for topological insulators and topological superconductors [58]. Topological superconductors may give rise to Majorana fermions [60], predicted by E. Majorana in 1937, but not yet found experimentally. Interest in these quasiparticles is related to the fact that they can theoretically be used as qubits in a topological quantum computer. In one-dimensional systems, we deal with Majorana localized states, or Majorana modes (MMs), which do not move freely in the system, rather than with Majorana fermions. Interest in one-dimensional systems is largely related to the one-dimensional Kitaev chain model [61], which is the simplest model that allows MMs to be described in the most visual form [58].

As a possible material for the implementation of Majorana states, Kitaev proposed to use nanowires made of a p-wave superconductor, i.e., one-dimensional superconductors with triplet states of Cooper pairs. This is why Ising superconductors with a triplet order parameter are of interest for

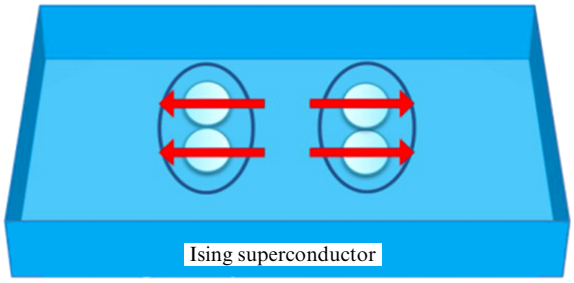

Figure 15. Spin-triplet Cooper pairs induced by Ising spin–orbit coupling [65].

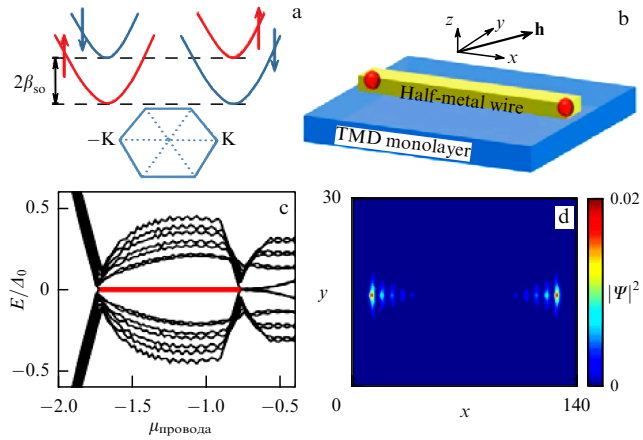

Figure 16. (a) Spectrum of electrons in MoS_2 in vicinity of K and −K points subject to Ising spin-split SOC fields. (b) Thin and long rod of a spin half-metal on surface of TMD monolayer. (c) Spectrum of the device (b) as a function of chemical potential of the wire. Red line shows topological regime with Majorana modes. (d) Wave function of ground topological state with zero energy. Maxima of spectral weight of Majorana fermions reside at ends of the wire [65].

the possible implementation of Majorana states. Several papers have examined the properties of long nanowires on a two-dimensional surface as the most favorable models for the implementation of MMs.

To this end, Yuan et al. [40] focused on investigating the electronic structure of a long superconducting strip of MoS_2. Figure 14 shows the electron spectra in the tight-binding model for a long thin strip of MoS_2.

Various exotic phases with edge states and Majorana flat bands are possible. However, to implement such exotic states, it is necessary that the chemical potential lie above the energy level at the M point of the Brillouin zone. As Yuan et al. [40] note, this regime for MoS_2 is unrealistic, since the chemical potential lies in the vicinity of the ±K points. It is possible that the predicted phases will be discovered for other TMDs. Chiral Majorana edge states in a hypothetical superconducting phase with a $d+id$ phase have also been predicted for graphene [62–64].

The orientation of the external magnetic field plays an important role in the formation of superconductivity in Ising superconductors. In the superconducting phase, the pair correlation function $F_\theta(\mathbf{k}, E)$ has the form [65]

$$F_\theta(\mathbf{k}, E) = \begin{pmatrix} -d_z\sin\theta & \psi_{\text{s}} + d_z\cos\theta \\ -\psi_{\text{s}} + d_z\cos\theta & d_z\sin\theta \end{pmatrix}. \qquad (5)$$

Here, ψ_{s} is a spin-singlet pair; d_z is a spin-triplet pair induced by the Ising SOC, $d_z \sim \beta_{\text{so}}$; and θ is the angle of the external

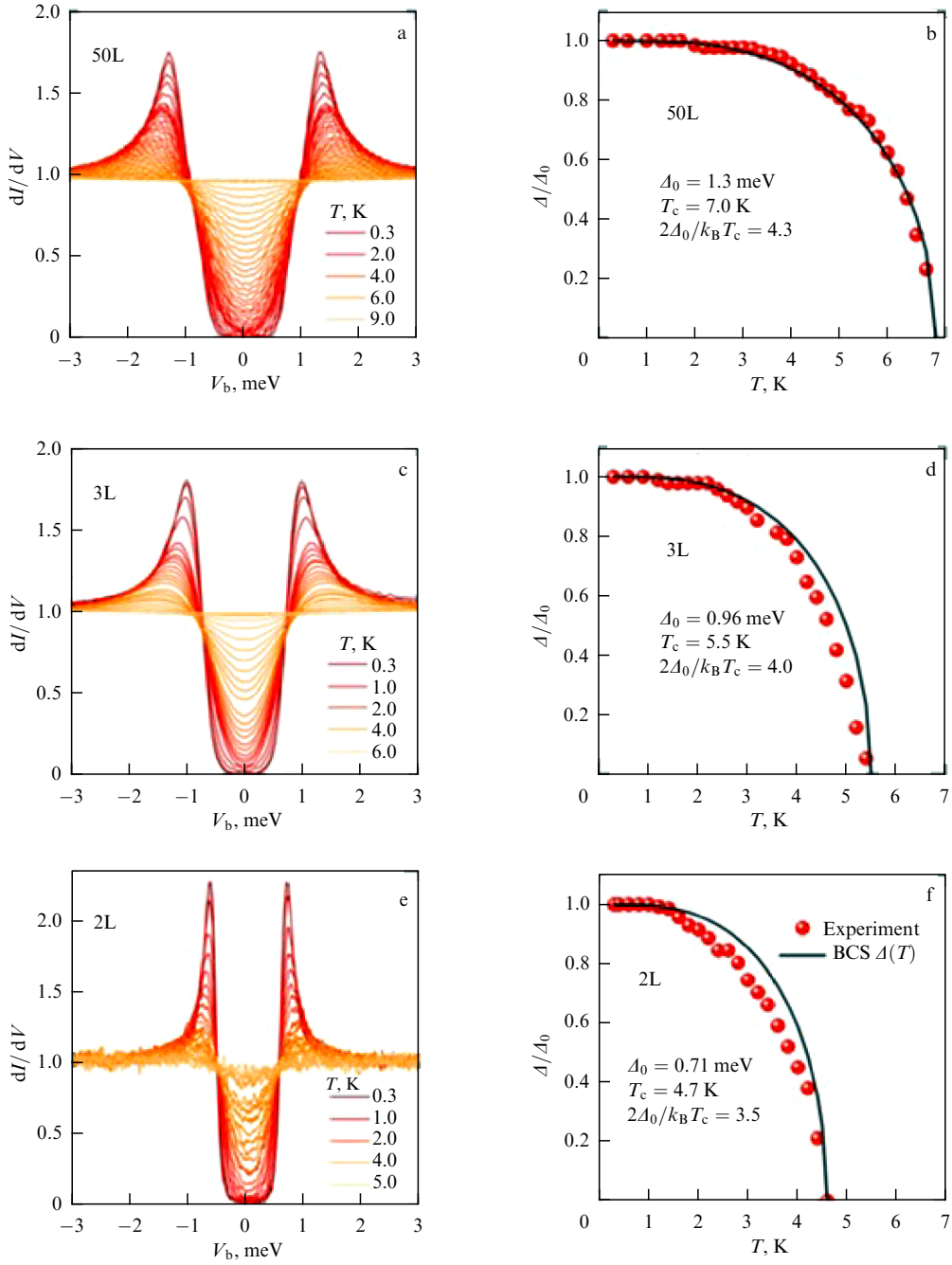

Figure 17. Temperature dependences of superconducting gap in few-layer $NbSe_2$ films. (a, c, e) Tunneling spectra at different temperatures and (b, d, f) temperature dependences of the gap in comparison with BCS theory [35].

magnetic field with the z-axis. If the external field lies across the plane of the layer, $\theta = 0$, then singlet and triplet pairs are present simultaneously, $F_{12} = \psi_s + d_z$. To orient the magnetic field in the plane of the sample, $\theta = \pi/2$, triplet pairs are formed by electrons with parallel spins in the plane of the sample (Fig. 15).

These states make it possible to detect Ising superconductivity and create Majorana fermions at the ends of a long rod of a spin half-metal placed on top of the TMD plane [65]. Recall that the term 'spin half-metal' is equivalent to the term 'half-metallic ferromagnet' [66]; the latter is mainly used in the Russian scientific literature [67]. In this state, the electron bands are spin split in such a way that, for one spin projection, the Fermi level lies in the band of allowed states, and for the other spin projection, the Fermi level lies in the forbidden band. The Majorana mode is nonuniformly distributed in a thin wire on the surface of the Ising superconductor (Fig. 16).

Possible scenarios for the formation of superconductivity with nontrivial topological phases in TMDs were also discussed in papers [68–70]. The possibilities of forming Majorana states and their manifestations in experiments are often discussed. As noted above, the specifics of the band structure of non-intrinsic MoS_2 and WS_2 superconductors, in which pockets near K points are responsible for conductivity at a low density of electrons injected by an external electric field, do not allow nontrivial topological superconductivity to be formed. However, in the intrinsic superconductors $NbSe_2$,

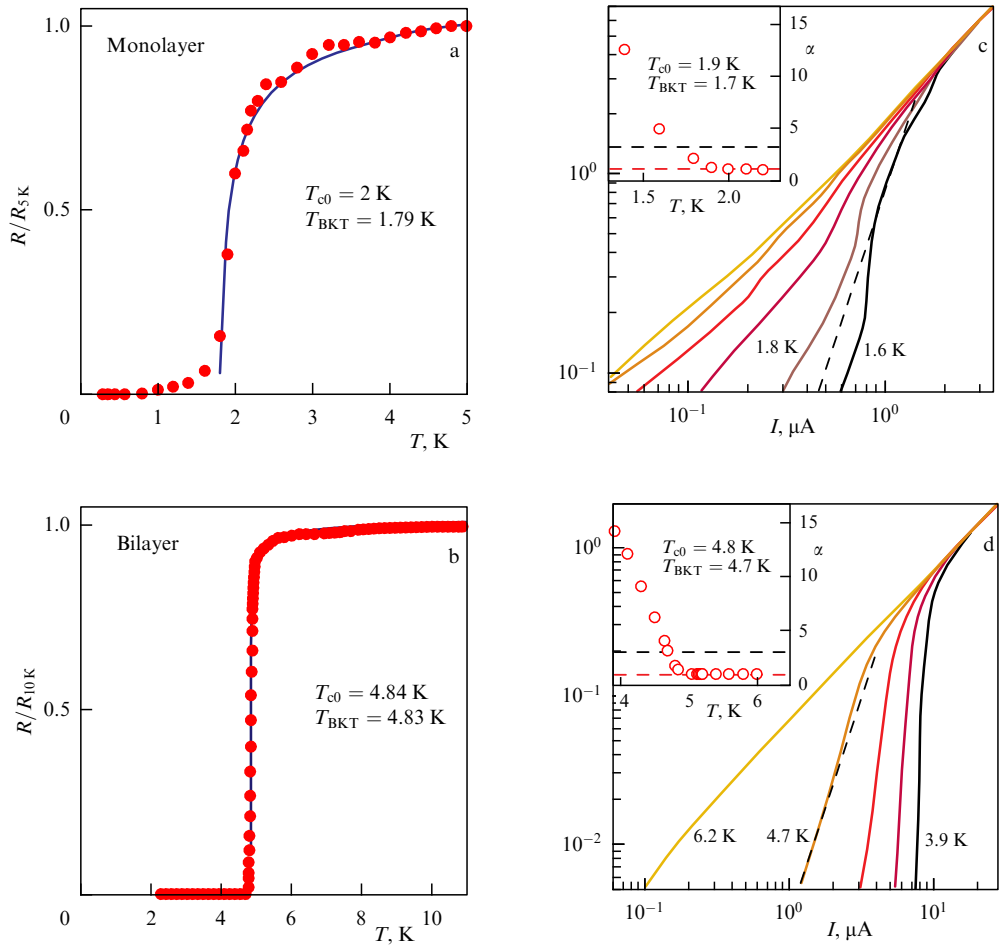

Figure 18. Role of BKT transition in $NbSe_2$. Temperature dependences of resistance in (a) monolayer and (b) bilayer samples; solid lines are described by Halperin–Nelson formula [52]. (c, d) Current–voltage characteristics for same samples; dashed lines corresponds to $V \sim I^{\alpha}$ with critical exponent $\alpha = 3$. Insets show temperature dependences of exponent α [35].

NbS_2, $TaSe_2$, and TaS_2, the situation is different, which gives hope for the implementation of nodal topological phases in these TMDs in the presence of an external magnetic field in the plane of the layer that is greater than the paramagnetic limit but less than H_{c2} [70].

5. Features of superconducting state in intrinsic $NbSe_2$-type superconductors

The group of compounds $NbSe_2$, NbS_2, $TaSe_2$, and TaS_2 includes undoped metals, in which intrinsic superconductivity is realized. These TMDs are largely used in many different experimental studies, which will be considered in this section. Note that superconductivity and the dielectric state of the charge-density wave (CDW) compete [7, 37]. For example, in bulk $NbSe_2$, the CDW state is formed below $T_{CDW} = 33$ K and superconductivity appears below $T_c = 7.2$ K. Below T_c, these two phases coexist. Ugeda et al. [71] used scanning tunneling microscopy/spectroscopy (STM/STS) and angle-resolved photoelectron spectroscopy (ARPES) to study experimentally the electronic properties of the $NbSe_2$ monolayer. They also measured the electrical transport properties. Superconductivity was observed in the monolayer, but T_c decreased to 1.9 K. A CDW phase with 3×3 ordering and a gap of 4 meV at the Fermi level was also detected at $T = 5$ K.

Using measurements of tunneling spectra and transport properties, Khestanova et al. [35] investigated fundamental problems of two-dimensional and quasi-two-dimensional superconductivity in $NbSe_2$ single crystals with a small number of layers. Superconductivity is usually suppressed in thin films with decreasing thickness. For example, superconductivity was suppressed by structural disorder in amorphous films [72, 73]. In contrast, single-crystal $NbSe_2$ films retain superconductivity with decreasing thickness to one monolayer. Figure 17 shows the temperature dependences of the superconducting gap for $NbSe_2$ films with different numbers of layers. Tunneling spectra at different temperatures (Fig. 17a) and temperature dependences of the gap (Fig. 17b) in comparison with the Bardeen–Cooper–Schrieffer (BCS) theory were obtained in [35].

Note that the T_c values determined from the tunneling spectra and from resistive measurements by the same authors coincide with an accuracy of ± 0.2 K. Khestanova et al. [35] also estimated the influence of thermal fluctuations caused by the formation and decay of Berezinskii–Kosterlitz–Thouless (BKT) vortex–antivortex pairs [74, 75]. The destruction of the vortex leads to additional dissipation, which in transport measurements looks like a resistive transition, although the superconducting state is still present in the substance. The BKT transition occurs at temperature $T_{BKT} < T_{c0}$, where T_{c0} is associated with the superconducting transition itself due to

the destruction of Cooper pairs. To clarify the role of the BKT transition in the observed decrease in T_c with a decreasing number of layers, Khestanova et al. [35] analyzed the temperature dependences of $R(T)$ and the $I-V$ characteristics of the thinnest samples with number of layers $N = 1$ and 2 (Fig. 18).

One way to determine T_{BKT} is to use the Halperin–Nelson method [76], which describes the resistance taking into account thermally excited vortices. Another method is based on the analysis of the critical exponent $V \sim I^{\alpha}$ for the voltage–current dependence proposed in [77], according to which

$$R(T) \approx 10.8cR\exp\left[-2\sqrt{\frac{c(T_{c0}-T_{BKT})}{T-T_{BKT}}}\right]. \qquad (6)$$

Here, T_{c0}, T_{BKT}, and the dimensionless constant c are adjustable parameters. As can be seen from Fig. 18, the difference between T_{c0} and T_{BKT} is no more than 0.2 K for a monolayer; for a bilayer sample, the indicated temperatures are practically indistinguishable. Similar results are obtained by analyzing the critical exponent α. According to [77], $\alpha = 3$ and 1 for $T = T_{BKT}$ and $T = T_{c0}$, respectively. As can be seen from Fig. 18, the results are almost identical and lead to the conclusion that $T_{BKT} \approx T_{c0}$ for both monolayer and bilayer samples. The proximity of these two temperatures is not accidental and is due to the quite large mean free path $l > \xi_0$ and the high carrier density $n \sim 10^{15}$ cm^{-2} per layer.

It should be noted that the above analysis of the results of paper [77] does not include the CDW phase, which coexists with the superconducting phase (see also [78, 79]). For $NbSe_2$ films with a small number of layers, an increase in T_{CDW} was found with a decrease in the number of layers, in contrast to a decrease in T_c [80]. Moreover, incommensurate CDW phases in $NbSe_2$ do not compete with superconductivity [79] and can even induce superconductivity [81].

As for the superconducting state of $NbSe_2$, all symmetry variants considered above in Section 3.3 are valid for it. Hamill et al. [82] studied experimentally the complex symmetry of superconducting pairing in samples with a small number of atomic layers and measured magnetoresistance and tunneling through the $NbSe_2/CrBr_3$ structure. Both experiments revealed a biaxial symmetry of the superconducting state, in contrast to the triaxial symmetry of the lattice. In both experiments, the biaxial anisotropy disappears in the normal phase. Hamill et al. [82] attributed the observed effects to the complex symmetry of the superconducting phase, namely to a superposition of the usual s-phase and the unusual d- or p-phase. As was shown in Section 3.3, the symmetry of TMDs allows this mixing, and the presence of a magnetic field can generate mixing of different phases, as can be seen from formula (5). Kuzmanović et al. [83] explain the features of the superconducting gap extracted from tunneling experiments in strong magnetic fields on the order of 30 T by the coexistence of singlet pairs and triplet pairs with parallel spins, as shown in Fig. 15.

6. Inhomogeneous magnetic states in Ising superconductors

Since the Ising and Rashba anisotropies in TMDs are in some sense equivalent to the internal magnetic field, inhomogeneous LOFF states can appear [84, 85]. For ordinary superconductors, spatial parity and time reversibility are preserved. In an external magnetic field, the violation of time reversibility leads to an inhomogeneous LOFF state with a nonzero wave vector **q**. In two-dimensional layers with the Rashba spin–orbit coupling and the Ising spin–orbit coupling with the removal of the degeneracy of the Fermi surface pockets around K and −K points, electron energy levels become split, and Cooper pairs with a nonzero total wave vector **q** can be formed. Wan et al. [86] considered the specifics of the LOFF states in Ising superconductors (Fig. 19). Pairing in the mth layer occurs with $\mathbf{k} - \mathbf{k}' = (-1)^m\mathbf{q}$.

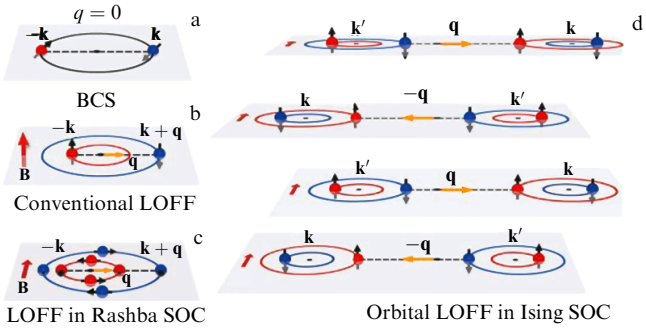

Figure 19. Specific features of Larkin–Ovchinnikov–Fulde–Ferrell states in Ising superconductors. (a) Conventional BCS pairing with zero momentum, (b) LOFF pairing with finite momentum due to Zeeman splitting, (c) LOFF pairing due to Rashba spin–orbit coupling, and (d) LOFF pairing in an Ising superconductor. (Borrowed from [86].)

Another option for creating inhomogeneous magnetic states was examined by Aikebaier et al. [87], who considered a model of a van der Waals heterostructure with ferromagnetic layers of CrI_3, $CrBr_3$, or $CrCl_3$ and superconducting layers of $NbSe_2$ Ising superconductors. Ising superconductivity makes it possible to control the magnetic state of the heterostructure. In such a van der Waals heterostructure, the interaction between the magnetic layers is formed by anisotropic spin susceptibility. Switching between two magnetic states occurs at a characteristic temperature T^* inside the superconducting phase with a change in the spin susceptibility of $NbSe_2$, formed by the Ising spin–orbit coupling (Fig. 20).

Such van der Waals superconductor/ferromagnet heterostructures may prove promising for developing superconducting spintronics devices.

7. Conclusions

In this review, we have limited ourselves mainly to TMDs with the 2H-MX_2 structure, since they are examined in the majority of publications. However, there are several studies on other structural types. Wang et al. [88] discussed the possibility of CDW formation and Ising superconductivity in a 1T-$HfTe_2$ monolayer. Peng et al. [89] studied type-II Ising superconductivity in the centrosymmetric 1T′-MoS_2 structure.

We would also like to discuss the question of why Ising superconductivity is realized in TMDs of the MX_2 composition with 4d elements M. Similar compositions with 3d elements M are also possible and were discussed in review [30] and book [90]. Disulfides of 3d metals can contain both monoatomic anions (S^{2-}) and molecular ones (S_2^{2-}) in their structure. Therefore, transition metal disulfides are divided

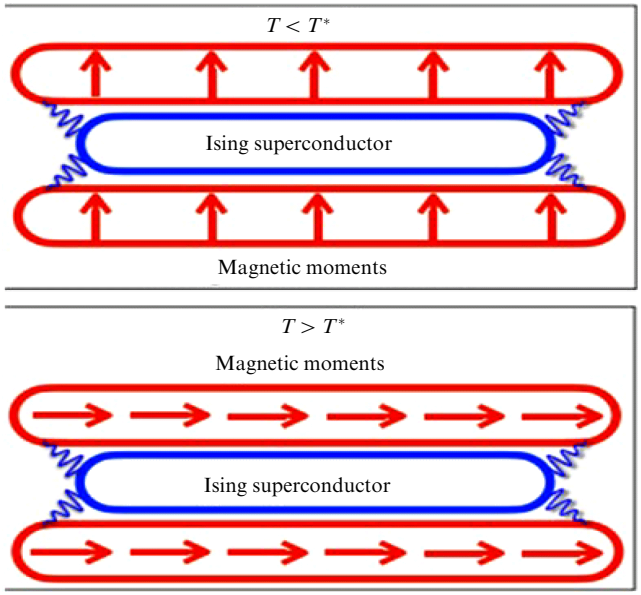

Figure 20. Schematic structure of a van der Waals heterostructure with alternating layers of a CrI_3 ferromagnetic dielectric and an Ising superconductor. For temperatures $T < T^*$, the ferromagnetic coupling is out-of-plane; for $T > T^*$, ferromagnetic coupling is in-plane. Here, $T^* < T_c$, i.e., reorientation of entire heterostructure occurs in superconducting phase of $NbSe_2$. (Borrowed from [87].)

into two main classes: layered with the structure CdI_2 and with the pyrite structure FeS_2 [91]. Layered CdI_2 lattices are constructed by parallel packing of I–Cd–I layers, just like S–Mo–S in MoS_2. In such crystals, two types of bonds dominate: electrostatic ones within the layers and van der Waals forces between the layers. However, the structure of the 4d-metal disulfides considered in this review differs from the hexagonal close-packed lattice in TiS_2 and VS_2, which are characterized by a deviation from stoichiometry and a transition to an NiAs-type structure with an excess of metal [92]. Forms of TiS_2 with a fullerene-like structure [93] and in the form of nanotubes [94] are also known. Stoichiometric TiS_2 is a metal and a Pauli paramagnet. Nonstoichiometric $V_{1+x}S_2$ ($x = 0.2$) is an antiferromagnetic metal. The magnetic properties of the dichalcogenides $MnSe_2$, $MnTe_2$, FeS_2, CoS_2, and NiS_2 with a face-centered cubic (fcc) structure of the $C2$ type are discussed in book [91]. This analysis showed that Ising superconductivity is currently limited only to layered structures MX_2 with 4d elements.

In conclusion, we note other nontrivial properties of two-dimensional triangular lattices of TMDs, in particular with a moiré lattice. The relationship between the Mott transition and the formation of a pseudogap is also actively studied in the Hubbard model for two-dimensional materials with a triangular lattice (moiré superlattices) such as transition metal dichalcogenides [95, 96].

Acknowledgments

Sections 1, 2, and 4 of this paper were written within the framework of the scientific topic of the state assignment of the L.V. Kirensky Institute of Physics of the Siberian Branch of the Russian Academy of Sciences. Sections 3, 5, 6, and 7 were written with the support of the Russian Science Foundation (grant no. 24-12-00044, https://rscf.ru/project/24-12-00044).

References

1. Novoselov K S et al. *Science* **306** 666 (2004)
2. Mineev V P, Samokhin K V *Introduction to Unconventional Superconductivity* (Amsterdam: Gordon and Breach Sci. Publ., 1999); Translated from Russian: *Vvedenie v Teoriyu Neobychnoi Sverkhprovodimosti* (Ser. Theoretical Physics) (Moscow: Izd. MFTI, 1998)
3. Chandrasekhar B S *Appl. Phys. Lett.* **1** 7 (1962)
4. Clogston A M *Phys. Rev. Lett.* **9** 266 (1962)
5. Gorter C J, Casimir H *Physica* **1** 306 (1934)
6. Saint-James D, Sarma G, Thomas E J *Type II Superconductivity* (Oxford: Pergamon Press, 1969); Translated into Russian: *Sverkhprovodimost' Vtorogo Roda* (Moscow: Mir, 1970)
7. Bulaevskii L N *Sov. Phys. Usp.* **18** 514 (1975); *Usp. Fiz. Nauk* **116** 449 (1975)
8. Bulaevskii L N *Sov. Phys. Usp.* **26** 544 (1983); *Usp. Fiz. Nauk* **140** 334 (1983)
9. Buzdin A I et al. *Sov. Phys. Usp.* **27** 927 (1984); *Usp. Fiz. Nauk* **144** 597 (1984)
10. Izyumov Yu A, Proshin Yu N, Khusainov M G *Phys. Usp.* **45** 109 (2002); *Usp. Fiz. Nauk* **172** 113 (2002)
11. Schmidt V V *The Physics of Superconductors: Introduction to Fundamentals and Applications* (Eds P Müller, A V Ustinov) (Berlin: Springer, 1997) Translated from 1st Russian ed.; Schmidt V V *Vvedenie v Fiziku Sverkhprovodnikov* 2nd Russian ed., rev. and enlarged (Moscow: MTsNMO, 2000)
12. Shalnikov A *Nature* **142** 74 (1938)
13. Chernozatonskii L A, Artyukh A A *Phys. Usp.* **61** 2 (2018); *Usp. Fiz. Nauk* **188** 3 (2018)
14. Kvashnin D G, Chernozatonskii L A *JETP Lett.* **105** 250 (2017); *Pis'ma Zh. Eksp. Teor. Fiz.* **105** 230 (2017)
15. Wang Q H et al. *Nat. Nanotechnol.* **7** 699 (2012)
16. Duerloo K-A N, Li Y, Reed E J *Nat. Commun.* **5** 4214 (2014)
17. Ye J T et al. *Science* **338** 1193 (2012)
18. Lu J M et al. *Science* **350** 1353 (2015)
19. Saito Y et al. *Nature Phys.* **12** 144 (2016)
20. Klemm R A *Layered Superconductors* Vol. 1 (Oxford: Oxford Univ. Press, 2012)
21. Xi X et al. *Nature Phys.* **12** 139 (2016)
22. de la Barrera S C et al. *Nat. Commun.* **9** 1427 (2018)
23. Xing Y et al. *Nano Lett.* **17** 6802 (2017)
24. Zhang R et al. *Nano Lett.* **16** 629 (2016)
25. Liu L et al. *Nature Mater.* **17** 1108 (2018)
26. Yu Y et al. *Nature Chem.* **10** 638 (2018)
27. Gor'kov L P, Rashba E I *Phys. Rev. Lett.* **87** 037004 (2001)
28. Frigeri P A et al. *Phys. Rev. Lett.* **92** 097001 (2004)
29. Zhou B T et al. *Phys. Rev. B* **93** 180501 (2016)
30. Wilson J A, Yoffe A D *Adv. Phys.* **18** 193 (1969)
31. Kuc A, Zibouche N, Heine T *Phys. Rev. B* **83** 245213 (2011)
32. Calandra M, Mazin I I, Mauri F *Phys. Rev. B* **80** 241108 (2009)
33. Lian C-S , Si C, Duan W *Nano Lett.* **18** 2924 (2018)
34. Frindt R *Phys. Rev. Lett.* **28** 299 (1972)
35. Khestanova E et al. *Nano Lett.* **18** 2623 (2018)
36. Keldysh L V, Kopaev Yu V *Sov. Phys. Solid State* **6** 2219 (1965); *Fiz. Tverd. Tela* **6** 2791 (1964)
37. Kopaev Yu V *Trudy Fiz. Inst. Akad. Nauk* **86** 3 (1975)
38. Zhang H et al. *Nature Phys.* **18** 1425 (2022)
39. Kormányos A et al. *Phys. Rev. B* **88** 045416 (2013)
40. Yuan N F Q, Mak K F, Law K T *Phys. Rev. Lett.* **113** 097001 (2014)
41. Bychkov Yu A, Rashba E I *JETP Lett.* **39** 78 (1984); *Pis'ma Zh. Eksp. Teor. Fiz.* **39** 66 (1984)
42. Ge Y, Liu A Y *Phys. Rev. B* **87** 241408 (2013)
43. Das S et al. *npj Comput. Mater.* **9** 66 (2023)
44. Das S, Mazin I I *Comput. Mater. Sci.* **200** 110758 (2021)
45. Wickramaratne D, Mazin I I *Appl. Phys. Lett.* **122** 240503 (2023)
46. Roldán R, Cappelluti E, Guinea F *Phys. Rev. B* **88** 054515 (2013)
47. Mackenzie A P, Maeno Y *Rev. Mod. Phys.* **75** 657 (2003)
48. Das Sarma S, Nayak C, Tewari S *Phys. Rev. B* **73** 220502 (2006)
49. Sato M, Fujimoto S *Phys. Rev. B* **79** 094504 (2009)
50. Bauer E, Sigrist M (Eds) *Non-Centrosymmetric Superconductors. Introduction and Overview* (Lecture Notes in Physics, Vol. 847) (Berlin: Springer-Verlag, 2012) https://doi.org/10.1007/978-3-642-24624-1

51. Yip S *Annu. Rev. Condens. Matter Phys.* **5** 15 (2014)
52. Haldane F D M *Phys. Rev. Lett.* **47** 1840 (1981)
53. Volovik G E *JETP Lett.* **66** 522 (1997); *Pis'ma Zh. Eksp. Teor. Fiz.* **66** 492 (1997)
54. Volovik G E *The Universe in a Helium Droplet* (Intern. Ser. of Monographs on Physics, Vol. 117) (New York: Oxford Univ. Press, 2009) https://doi.org/10.1093/acprof:oso/9780199564842.001.0001
55. Hasan M Z, Kane C L *Rev. Mod. Phys.* **82** 3045 (2010)
56. Tarasenko S A *Phys. Usp.* **61** 1026 (2018); *Usp. Fiz. Nauk* **188** 1129 (2018)
57. Pankratov O A *Phys. Usp.* **61** 1116 (2018); *Usp. Fiz. Nauk* **188** 1226 (2018)
58. Val'kov V V et al. *Phys. Usp.* **65** 2 (2022); *Usp. Fiz. Nauk* **192** 3 (2022)
59. Schnyder A P et al. *Phys. Rev. B* **78** 195125 (2008)
60. Majorana E *Nuovo Cimento* **14** 171 (1937)
61. Kitaev A Yu *Phys. Usp.* **44** (10S) 131 (2001); *Usp. Fiz. Nauk* **171** (Suppl. 10) 131 (2001)
62. Black-Schaffer A M, Doniach S *Phys. Rev. B* **75** 134512 (2007)
63. Nandkishore R, Levitov L S, Chubukov A V *Nature Phys.* **8** 158 (2012)
64. Black-Schaffer A M *Phys. Rev. Lett.* **109** 197001 (2012)
65. Zhou B T et al. *Phys. Rev. B* **93** 180501 (2016)
66. de Groot R A et al. *Phys. Rev. Lett.* **50** 2024 (1983)
67. Irkhin V Yu, Katsnel'son M I *Phys. Usp.* **37** 659 (1994); *Usp. Fiz. Nauk* **164** 705 (1994)
68. Hsu Y-T et al. *Nat. Commun.* **8** 14985 (2017)
69. Oiwa R, Yanagi Y, Kusunose H *Phys. Rev. B* **98** 064509 (2018)
70. He W-Y et al. *Commun. Phys.* **1** 40 (2018)
71. Ugeda M M et al. *Nature Phys.* **12** 92 (2016)
72. Yazdani A, Kapitulnik A *Phys. Rev. Lett.* **74** 3037 (1995)
73. Hebard A F, Paalanen M A *Phys. Rev. Lett.* **65** 927 (1990)
74. Berezinskii V L *Sov. Phys. JETP* **32** 493 (1971); *Zh. Eksp. Teor. Fiz.* **59** 907 (1971)
75. Kosterlitz J M, Thouless D J *J. Phys. C* **6** 1181 (1973)
76. Halperin B I, Nelson D R *J. Low Temp. Phys.* **36** 599 (1979)
77. Nelson D R, Kosterlitz J M *Phys. Rev. Lett.* **39** 1201 (1977)
78. Valla T et al. *Phys. Rev. Lett.* **92** 086401 (2004)
79. Rahn D J et al. *Phys. Rev. B* **85** 224532 (2012)
80. Xi X et al. *Nat. Nanotechnol.* **10** 765 (2015)
81. Kiss T et al. *Nature Phys.* **3** 720 (2007)
82. Hamill A et al. *Nature Phys.* **17** 949 (2021)
83. Kuzmanović M et al. *Phys. Rev. B* **106** 184514 (2022)
84. Fulde P, Ferrel R A *Phys. Rev.* **135** A550 (1964)
85. Larkin A I, Ovchinnikov Yu N *Sov. Phys. JETP* **20** 762 (1965); *Zh. Eksp. Teor. Fiz.* **47** 1136 (1964)
86. Wan P et al. *Nature* **619** 46 (2023)
87. Aikebaier F, Heikkilä T T, Lado J L *Phys. Rev. B* **105** 054506 (2022)
88. Wang D, Wu J, Si C *Nano Res.* **16** 11521 (2023)
89. Peng J et al. *Adv. Mater.* **31** 1900568 (2019)
90. Goodenough J B *Magnetism and the Chemical Bond* (Interscience Monographs on Chemistry: Inorganic Chemistry Sect., Vol. 1) (New York: Interscience Publ., 1963); Translated into Russian: *Magnetizm i Khimicheskaya Svyaz'* (Moscow: Metallurgiya, 1968)
91. Loseva G V, Ovchinnikov S G, Petrakovskii G A *Perekhod Metall–Dielektrik v Sul'fidakh 3d-Metallov* (Metal–Dielectric Transition in 3d-Metal Sulfides) (Novosibirsk: Nauka, 1983)
92. Narai-Szabo I *Inorganic Crystal Chemistry* (Budapest: Publishing House of the Academy of Sciences of the Hungarian People's Republic, 1969)
93. Margolin A et al. *Chem. Phys. Lett.* **411** 162 (2005)
94. Chen J et al. *Chem. Commun.* (8) 980 (2003)
95. Wu F et al. *Phys. Rev. Lett.* **121** 026402 (2018)
96. Wu F et al. *Phys. Rev. Lett.* **122** 086402 (2019)